Electronic Supplementary Material (ESI) for Soft Matter.
This journal is © The Royal Society of Chemistry 2022

Dense packings of geodesic hard ellipses on a sphere:

SUPPLEMENTAL MATERIAL

Andraž Gnidovec and Simon Čopar

Faculty of Mathematics and Physics,

University of Ljubljana, Ljubljana, Slovenia

Anže Božič

Department of Theoretical Physics, Jožef Stefan Institute, Ljubljana, Slovenia

(Dated: September 1, 2022)

I. CONTACT HISTOGRAMS

In the main text we show that the mean contact number $\langle Z \rangle$ changes considerably with varying aspect ratio ε of spherical ellipses in dense packings. In Fig. S2 we plot the distributions of contacts (averaged over all generated packings) for systems of $N = 30$ and $N = 300$ particles at different aspect ratios to shed light on the effect of curvature on them. The tolerance value in the overlap function to detect a contact is again set at $\delta\lambda = 10^{-4}$. For both system sizes at $\varepsilon = 1$, circles with four contacts are the most common and there are no particles with 6 or more contacts, as the exact hexagonal packing cannot be achieved on a sphere. As we increase ε towards the peak of $\langle Z \rangle$ at $\varepsilon \approx 2$, the center of contact distribution moves towards $\varepsilon = 6$. Already at this point, some differences emerge between the $N = 30$ and $N = 300$ cases. The lower mean contact number $\langle Z \rangle$ for $N = 30$ observed in Fig. 2b can be traced back to the higher number of five-contact ellipses as opposed to the $N = 300$ case where six-contact ellipses dominate. With an increase in ε, contact distributions in both systems sizes widen significantly and the percentage of ellipses with fewer than six contacts increases. This is related to the formation of domains of parallel ellipse where neighboring parallel ellipses can be stabilized by four contacts in the case of large systems or even by only three contacts for small N where curvature is significant. Ellipses with high contact numbers can be found at the boundaries of these domains, lying approximately perpendicular to the parallel ellipses in the domain.

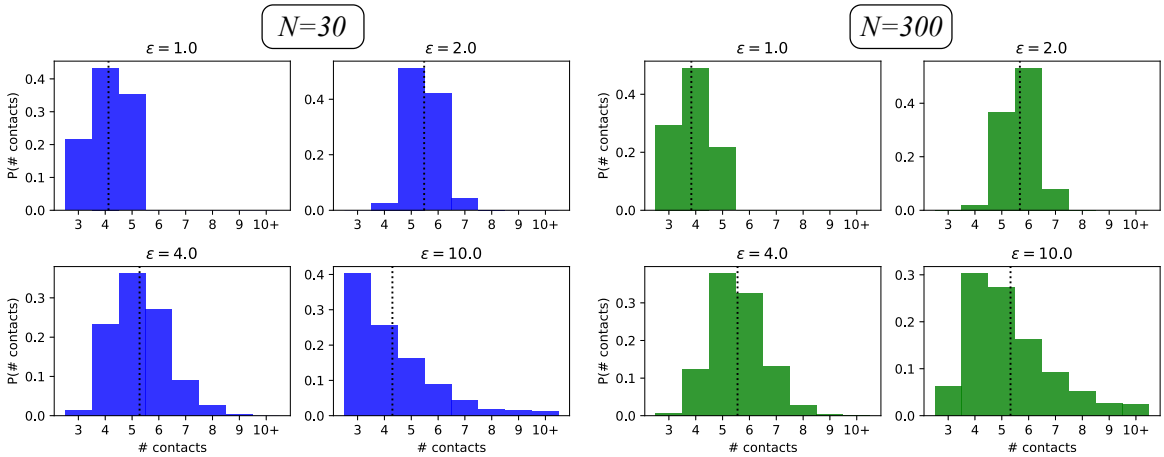

FIG. S1. Histograms of the number of contacts per ellipse for systems of $N = 30$ and $N = 300$ particles at different aspect ratios. Dotted vertical lines show the mean number of contacts $\langle Z \rangle$.

II. PACKING FRACTION CLOSE TO $\varepsilon = 1$

Our packing results for circle packing ($\varepsilon = 1$) are closely related to the Tammes problem of finding the densest packing configuration. Due to the strong frustration in the packing of circles on a surface with nonzero Gaussian curvature, the packing density of the optimal solution can change significantly with the number of particles, especially at lower N [1]. In our simulation, the Tammes solutions represent the upper density limit for RCP results. Nonetheless, this still influences the average packing density among generated configurations at different system sizes. One can see in Fig. S2 that better packing densities can be achieved for $N = 20$, 24, 30, 32, 36, 38, 44 and 48. Many of these values can be related to configurations with possible high-density structures with high symmetry, e.g., octahedral for $N = 24$ and 48—however, symmetry in itself is not a prerequisite for best packing [1]. The fluctuations in packing density decrease with an increase in N as adding additional particles into the system becomes less significant. When ε is increased from 1 (perturbations of spherical shape towards ellipsoids), the packing densities start to increase for all N, as discussed in the main text, but the peaks in N persist until $\varepsilon \approx 1.2 - 1.3$. In this region,

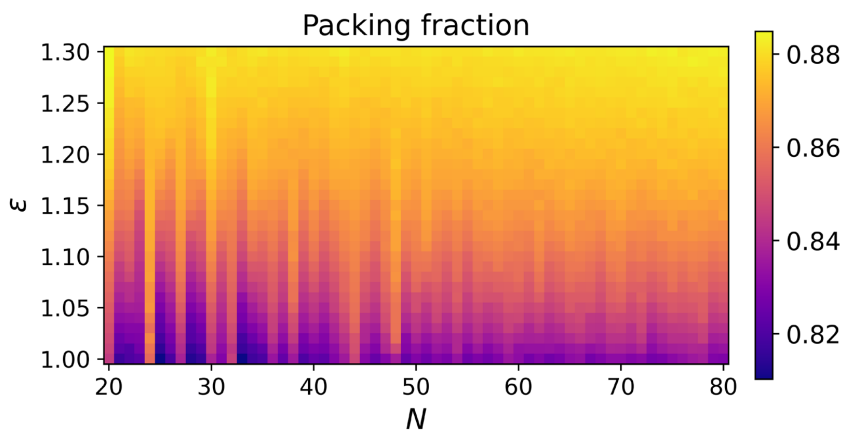

FIG. S2. Heatmap of the average packing density $\langle\phi\rangle$ in dependence to system size N and ellipse aspect ratio ϵ, with a focus on the range of ϵ close to 1. The average is taken over 30 generated configurations at each point (N, ε).

the packing density becomes mostly independent of N, demonstrating that more degrees of freedom lead to less frustrated packings compared to circles. Note again that for each pair (N, ε), we start from random initial conditions, so the solutions for $\varepsilon > 1$ are not simply propagated from $\varepsilon = 1$ results.

III. ENVELOPE OF PEAK WIDENING IN THE STRUCTURE FACTOR

As discussed in the main text, the widening of the peaks in the positional order (scalar) structure factor S_ℓ is related to the increase of possible distances between the centers of neighboring ellipses as the ellipse aspect ratio increases. The two edge cases are $d_{n.n.} = 2\beta$ (side by side ellipses) and $d_{n.n.} = 2\alpha$ (linearly arranged ellipses touching at apexes), with other touching configurations assuming intermediate values. Positions of the peaks in the structure factor can be linked to the minimal distance between neighboring particles,

$$\ell_k(d_{n.n.}) = \frac{2k\pi}{d_{n.n.}} \tag{S1}$$

where $k = 1, 2, 3, \ldots$ is the index of the peak [2]. Therefore, an increased range of possible distances amplifies an increasing number of S_ℓ, resulting in the widening of structure factor peaks and a decrease of their magnitudes. We would like to calculate an expression for the envelope of amplified ℓ_k in dependence to the system size and aspect ratio, with left and right branches $\ell^{(l)}_{\text{crit}}(N, \varepsilon) = \ell_k(2\alpha)$ and $\ell^{(r)}_{\text{crit}}(N, \varepsilon) = \ell_k(2\beta) = \ell_k(2\alpha/\varepsilon)$, respectively. This calls for an expression for $\alpha(N, \varepsilon)$ in a dense packing that can be obtained from the packing fraction $\phi(N, \varepsilon) = NA/4\pi$ if we approximate the ellipse area by $A(\alpha, \varepsilon) = \pi\alpha\beta = \pi\alpha^2/\varepsilon$. While this expression is not derived from the exact formula [Eq. (1)], Fig. S3 shows that it

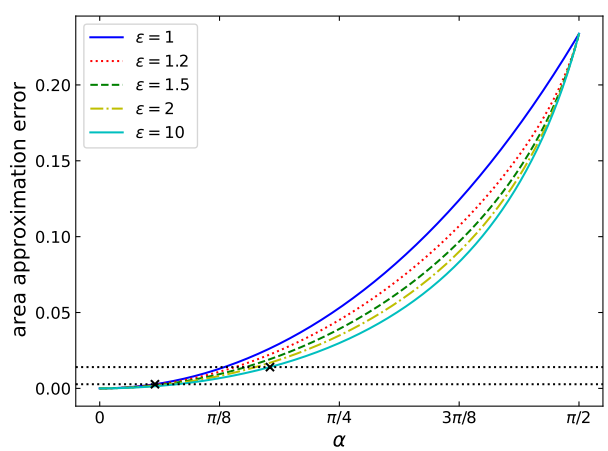

FIG. S3. Relative error of approximating the ellipse area as $A = \pi\alpha^2/\varepsilon$ instead of the expression in Eq. (1) in the main text, as a function of the ellipse size α and shown for different ellipse aspect ratios ε. Black markers and horizontal lines show the error for $N = 100$ ellipses with $\varepsilon = 1$ (left marker) and $\varepsilon = 10$ (right marker).

works well for large N where the ellipse sizes are small (the error is on the order of a few percent). We get $\alpha = \sqrt{4\varepsilon\phi(\varepsilon)/N}$ and thus

$$\ell^{(l)}_{\rm crit}(N,\varepsilon) = k\pi\sqrt{\frac{N}{4\varepsilon\phi(\varepsilon)}}, \qquad \ell^{(r)}_{\rm crit}(N,\varepsilon) = k\pi\sqrt{\frac{N\varepsilon}{4\phi(\varepsilon)}}, \tag{S2}$$

for the left and the right branch of the k-th envelope. As the dependence of packing fraction on N is weak, we neglect it in expressions (S2), resulting in $\ell_{\rm crit} \propto \sqrt{N}$.

IV. TENSOR HAMONIC EXPANSION

Let $T = T^{ij}\boldsymbol{e}_i \otimes \boldsymbol{e}_j$ be a traceless symmetric tensor field on the surface of a unit sphere, i.e., we have $T^{ij} = T^{ji}$ and $T^{ii} = -T^{jj}$, and the vectors $\boldsymbol{e}_i \in \{\boldsymbol{e}_\vartheta, \boldsymbol{e}_\varphi\}$ form an orthonormal basis on the sphere. Basis tensors for the harmonic expansion of this field can be obtained by acting on spherical harmonics $Y_{\ell m}$ with operators $\boldsymbol{\nabla}_s\boldsymbol{\nabla}_s$, $\boldsymbol{L}_s\boldsymbol{L}_s$, and $\boldsymbol{\nabla}_s\boldsymbol{L}_s$, where $\boldsymbol{\nabla}_s = \widehat{\boldsymbol{\vartheta}}\partial_\vartheta + \widehat{\boldsymbol{\varphi}}\frac{1}{\sin\vartheta}\partial_\varphi$ and $\boldsymbol{L}_s = \boldsymbol{r}\times\boldsymbol{\nabla} = \widehat{\boldsymbol{\varphi}}\partial_\vartheta - \widehat{\boldsymbol{\vartheta}}\frac{1}{\sin\vartheta}\partial_\varphi$ [3, 4]. After some algebraic manipulation, we get two orthonormal basis tensors,

$$t^+_{\ell m} = -\imath\left[2\ell(\ell+1)(\ell-1)(\ell+2)\right]^{-1/2}\begin{pmatrix} -X_{\ell m} & W_{\ell m} \\ W_{\ell m} & X_{\ell m}\end{pmatrix}, \tag{S3}$$

$$t^\times_{\ell m} = \left[2\ell(\ell+1)(\ell-1)(\ell+2)\right]^{-1/2}\begin{pmatrix} W_{\ell m} & X_{\ell m} \\ X_{\ell m} & -W_{\ell m}\end{pmatrix}, \tag{S4}$$

with $X_{\ell m} = \frac{2}{\sin\vartheta}\partial_\varphi\left(\partial_\vartheta - \cot\vartheta\right)Y_{\ell m}$ and $W_{\ell m} = \left[\partial_{\vartheta\vartheta} - \frac{1}{\sin^2\vartheta}\partial_{\varphi\varphi} - \frac{\cos\vartheta}{\sin\vartheta}\partial_\vartheta\right]Y_{\ell m}$. Note that the derivatives of $Y_{\ell m}$ can be expressed in terms of other spherical harmonics with the same ℓ. Tensor field T can then be expanded in terms of $t^+_{\ell m}$ and $t^\times_{\ell m}$ as

$$T = \sum_{\ell,m}\left(A_{\ell m}t^+_{\ell m} + B_{\ell m}t^\times_{\ell m}\right), \tag{S5}$$

with the expansion coefficients given by

$$A_{\ell m} = (T, t^+_{\ell m}) = \int \mathrm{d}\Omega\, T^* : t^+_{\ell m}, \tag{S6}$$

and equivalently for $B_{\ell m}$. (Here, the dot product of two tensors is defined as $T : S = T^{ij}S_{ij}$.) From these coefficients, we define the tensor structure factor for t^+ and $t^\times$ components analogously to the scalar structure factor,

$$S^+_\ell = \frac{4\pi}{N}\frac{1}{2\ell+1}\sum_{m=-\ell}^{\ell}|A_{\ell m}|^2, \qquad S^\times_\ell = \frac{4\pi}{N}\frac{1}{2\ell+1}\sum_{m=-\ell}^{\ell}|B_{\ell m}|^2. \tag{S7}$$

We describe the configurations of ellipses on the sphere with a tensor field $Q(\Omega) = \sum_{k=1}^{N}[\hat{\boldsymbol{p}}_k \otimes \hat{\boldsymbol{p}}_k - I/2]\delta(\Omega - \Omega_k)$, where the ellipse orientations $\hat{\boldsymbol{p}}_k$ are given in the basis $\{\boldsymbol{e}_\vartheta, \boldsymbol{e}_\varphi\}$ and Ω_k are the ellipse positions in terms of polar and azimuthal angles. Panels (a) and (b) of Fig. S4 show the tensor structure factors S_ℓ^+ and $S_\ell^\times$, respectively, for packings with $N = 100$ particles. As in the case of the scalar harmonic expansion of positional order, presented in Sec. 4.1 in the main text, the results are averaged over all generated packings to smooth out variations and amplify common properties. For the packing of circles ($\varepsilon = 1$), we are effectively calculating the expansion of a random tensor field which gives a constant value of $S_\ell^+ = S_\ell^\times = 1/4$. As soon as $\varepsilon > 1$, some orientational order emerges in the packing that is expressed differently in the S_ℓ^+ and $S_\ell^\times$ structure factors. (Note that the S_ℓ^+ heatmap has a cutoff at 0.5 to improve contrast.)

At low ε, the behavior of the two structure factors differs mostly at low ℓ, where S_ℓ^+ has a minimum (but does not vanish) while $S_\ell^\times$ has a peak. Around the first peak of the scalar structure factor (Fig. 5 in the main text), both tensor expansions also have a local maximum, and each subsequent spectral peak is lower in intensity. Around $\varepsilon \approx 1.5$, the low ℓ behavior of S_ℓ^+ completely changes—for higher aspect ratios, we get a maximum at $\ell = 2$, and after the first peak, the structure factor quickly reaches the asymptotic value of 1/4. Conversely, the $S_\ell^\times$ structure factor (Fig. S4) shows a much richer behavior, with multiple spectral peaks emerging when the ellipse aspect ratio is increased. The positions of these peaks in the (ℓ, ε) plane can be related to the intersections of envelope branches with different peak indices k [Eq. (S1)]. The right branch with index k and the left branch with index $k + 1$ intersect at

$$(\varepsilon_k, \ell_k) = \left(\frac{k+1}{k}, \sqrt{\frac{k(k+1)N\pi^2}{4\phi(\varepsilon_k)}} \right). \tag{S8}$$

We determine the peak values ℓ_k and ε_k numerically from heatmaps in the (ℓ, ε) plane and plot the peak coordinates with respect to system size N in panels (c) and (d) of Fig. S4. Both coordinates follow the predicted N dependence—ε_k are constant, though slightly higher than the values for branch intersections, and ℓ_k are fitted well by a $\sqrt{N}$ function. Approximating constant $\phi(\varepsilon)$, one can also calculate the inverse function $\varepsilon_k(\ell_k)$. As shown in panel (b) of Fig. S4, the expansion of the inverse function up to the second order in ℓ, $\varepsilon_k(\ell_k) = 1 + A/\ell + B/\ell^2$ can be fitted well on the peak positions for the fit parameters A and B.

To understand the meaning behind the peaks in the $S_\ell^\times$ structure factor and the reasons

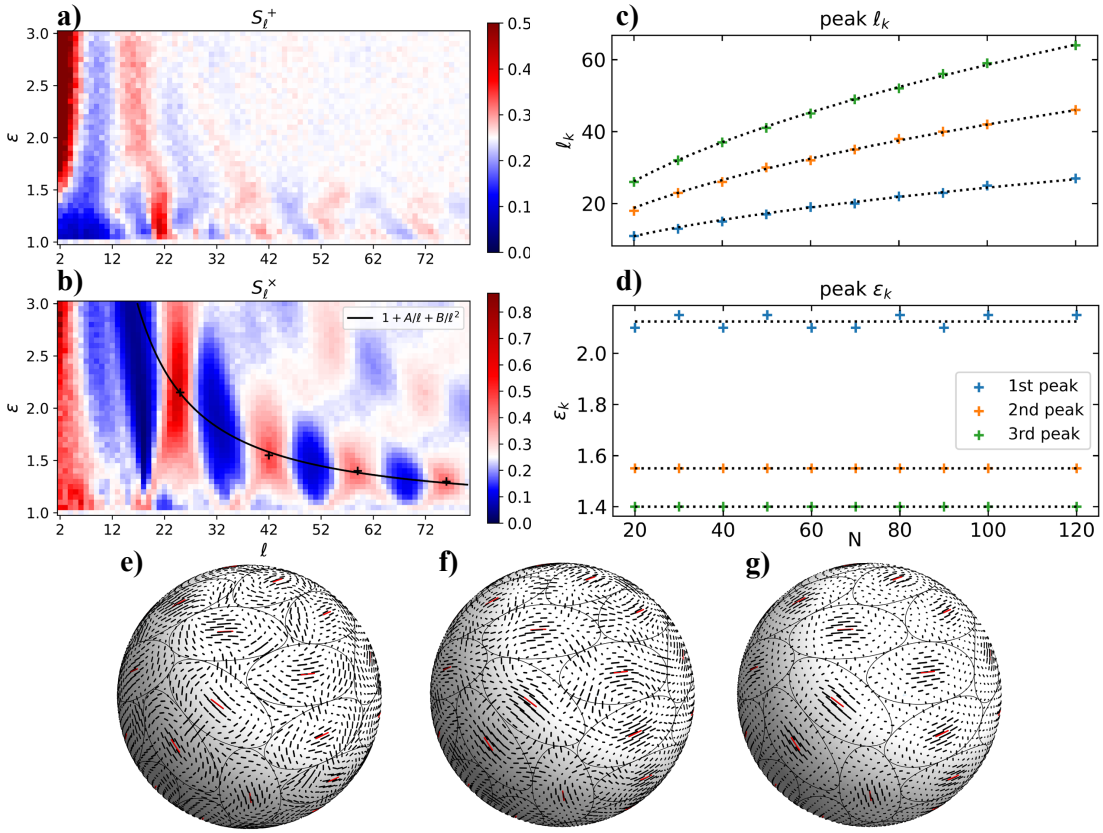

FIG. S4. **(a, b)** Heatmaps of the tensor structure factors S_ℓ^+ and $S_\ell^\times$ for configurations with $N = 100$ and $\varepsilon \in [1, 3]$. White color represents the asymptotic spectral value of $1/4$. Additionally, the heatmap for S_ℓ^+ has a cutoff at $S_\ell^+ = 0.5$ to increase the contrast in the plot. In panel (b), we fit the theoretically predicted function $\varepsilon_k(\ell)$ to the positions of the structure factor peaks. **(c, d)** Dependence of peak values ℓ_k and ε_k on system size N. We again fit the theoretical predictions, $\ell_k \propto \sqrt{N}$ and $\varepsilon_k = \text{const}$. **(e–g)** Interpolations of the ellipse tensor field based on the tensor expansion for a representative packing configuration with $N = 40$ and $\varepsilon = 2$, showing separately the interpolations of the S_ℓ^+ expansion (panel (e)) from the coefficients $A_{\ell m}$ and of the $S_\ell^\times$ expansion (panel (f)) from the coefficients $B_{\ell m}$, as well as the total expansion (panel (f)), given by the expression in Eq. (S5). For the interpolations shown in panels (e–g), the expansion was cut off at the position of the minimum after the first peak in $S_\ell^\times$.

behind why they do not appear in S_ℓ^+, we plot the interpolations of the tensor expansion on the entire sphere, calculated from the coefficients $A_{\ell m}$ and $B_{\ell m}$, both separately for the $+$ and $\times$ harmonics as well as for the whole expansion (panels (e–g) in Fig. S4). We use a configuration with $N = 40$ ellipses so that the structures in the plot are larger, and we

truncate the expansion at the minimum after the first peak in $S_\ell^\times$, essentially creating a low-pass filter. The expansion becomes less relevant at high ℓ, as we mostly get the echoes of features up to the right critical branch $\ell_{\rm crit}^{(r)}$. We observe that while both expansion components align with ellipse orientations near their centers, the typical length-scale at which the orientations in the interpolation change is larger for the $\times$ component that forms vortex-like structures for parallel neighboring ellipses with a vanishing tensor field in the vortex centers. At $\varepsilon \approx 2$ where two side-by-side ellipses match a single ellipse in length, it is possible for these vortex structures to be commensurate with the positional lattice, giving rise to the resonances observed in $S_\ell^\times$. Between ellipse centers, the $+$ spectral component is perpendicular to the orientation of the $\times$ component, which leads to a vanishing tensor filed for the full tensor expansion interpolation (panel (g) of Fig. S4). The delta functions at the ellipse centers become more pronounced if we include a larger number of expansion coefficients (higher cutoff value for the low-pass filter).

V. GEODESIC SPHERICAL ELLIPSES VS 3D ELLIPSOIDS

We compare the contact function between two geodesic spherical ellipses to the contact function between two prolate 3D ellipsoids at the same positions and orientations. The main ellipsoid axis is oriented tangential to the surface of the sphere, parallel to the orientation of the spherical ellipse, and the three semiaxes are of lengths $x_1 = \sin\alpha$ and $x_2 = x_3 = \sin\alpha/\varepsilon$, i.e., the spherical ellipse and the ellipsoid have the same projections to the equatorial plane (Fig. 1 in the main text). We calculate both the true contact function between ellipsoids (Perram-Wertheim contact function [5]) as well as the approximation by Berne and Pechukas [6] for all possible orientations ϕ_0 and ϕ_1 of the ellipse/ellipsoid pair, evaluated at a given geodesic distance γ. All the contact functions can be interpreted in terms of a scaling factor needed for ellipses/ellipsoids to reach tangency. This means that even though the values of 2D and 3D contact functions are not directly comparable as they are mapped over different spaces, in all cases the value of the contact function $\lambda = 1$ signifies that the particles are exactly touching. This allows us to compare the contours at level 1 in the plane of all possible mutual orientations of two ellipses at different geodesic distances γ, as shown in Fig. S5. The distances are chosen depending on the ellipse size α and aspect ratio ε, covering evenly the whole range from the distance where ellipses overlap for almost all

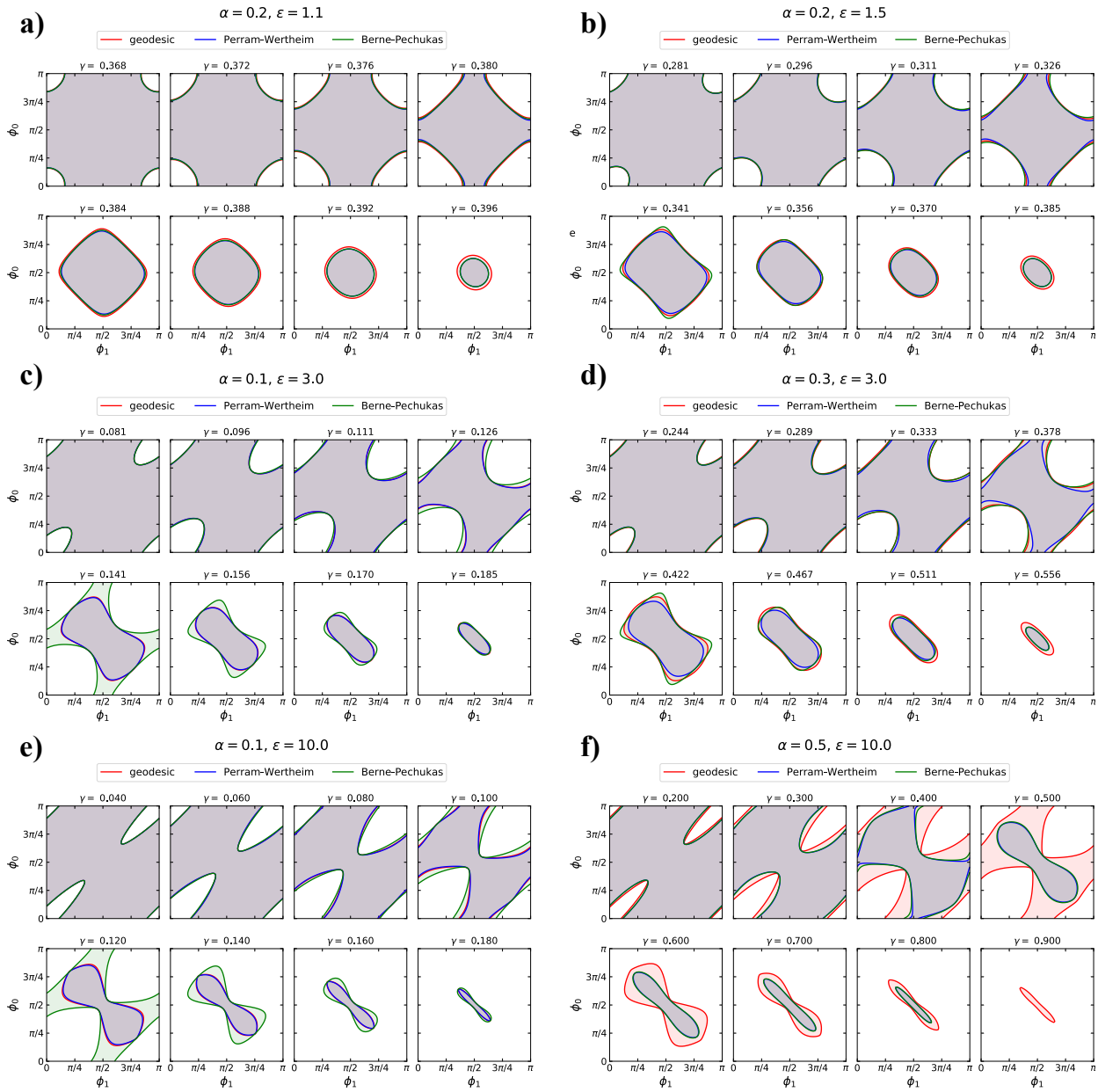

FIG. S5. Comparison between the contact function for geodesic spherical ellipses, the exact Perram-Wertheim contact function for ellipsoids and the Berne-Pechukas approximation, for different particel sizes α and aspect ratios ε. Colored lines show contours at level 1 (ellipses/ellipsoids touch in one point) for each contact function, in dependence to the orientations ϕ_0 and ϕ_1 of the first and second ellipse in the pair at a given geodesic distance γ. When $\phi_0 = \phi_1 = 0$, ellipses are aligned along the semi-major axes. Shaded area inside the contours shows the region in the orientation space where ellipses/ellipsoids overlap according to each contact function.

angles ϕ_0 and ϕ_1 to the distance where they touch only at very specific orientations.

At small ε, all three contact functions show good agreement on the overlap area in the orientation plane, as demonstrated in panels (a) and (b) of Fig. S5. Unsurprisingly, at large distances γ, the two ellipsoid contact functions show smaller overlap area (i.e., in general, measuring somewhat larger distance between ellipsoids than between spherical ellipses) as a consequence of scaling in 3D instead of on the curved spherical surface. Increasing particle aspect ratio ε, the differences between the contact functions become more pronounced. At small particle sizes (panels (c) and (e)), the spherical ellipse contact function still almost exactly matches the Perram-Wertheim contact function for ellipsoids; however, the Berne-Pechukas approximation shows large deviations from the two. At intermediate geodesic distances γ between the particle centers, it leads to much larger area where contact is detected. This can be related to the fact that Berne-Pechukas approximation can overestimate the correct touching distance [7, 8] and can lead to worse packing density in RCPs. For large particle sizes and large ε, the difference between geodesic ellipse and Perram-Wertheim ellipsoid contact function also increases, as shown in panel (d), where the geodesic ellipse contact function determines contacts similarly to the Berne-Pechukas approximation. For very oblong particles that are not small compared to the sphere radius (panel (f)), the differences between spherical ellipses and ellipsoids become large. The ellipsoids will mostly touch outside the spherical surface, which leads to a smaller area in the orientation plane where overlap is detected, leading to denser packing results. This relationship between overlap area and packing density can be considered in general—the contact function with larger area of detected overlaps will give lower packing densities.

---

[1] B. W. Clare and D. L. Kepert, *J. Math. Chem.*, 1991, **6**, 325–349.

[2] A. Božič and S. Čopar, *Phys. Rev. E*, 2019, **99**, 032601.

[3] F. J. Zerilli, *J. Mat. Phys.*, 1970, **11**, 2203–2208.

[4] K. S. Thorne, *Rev. Mod. Phys.*, 1980, **52**, 299.

[5] J. W. Perram and M. Wertheim, *J. Comput. Phys.*, 1985, **58**, 409–416.

[6] B. J. Berne and P. Pechukas, *J. Chem. Phys.*, 1972, **56**, 4213–4216.

[7] D. J. Cleaver, C. M. Care, M. P. Allen and M. P. Neal, *Phys. Rev. E*, 1996, **54**, 559–567.

[8] L. Paramonov and S. N. Yaliraki, *J. Chem. Phys.*, 2005, **123**, 194111.